

1 Far ultraviolet aurora identified at comet 67P/Churyumov- 2 Gerasimenko

3 M. Galand¹, P. D. Feldman², D. Bockelée-Morvan³, N. Biver³, Y.-C. Cheng³, G. Rinaldi⁴, M. Rubin⁵,
4 K. Altwegg⁵, J. Deca^{6,7}, A. Beth¹, P. Stephenson¹, K. L. Heritier¹, P. Henri⁸, J. Wm. Parker⁹,
5 C. Carr¹, A. I. Eriksson¹⁰, & J. Burch¹¹

6 ¹*Department of Physics, Imperial College London, Prince Consort Road, London, SW7 2AZ, UK*

7 ²*Department of Physics and Astronomy, The Johns Hopkins University, 3400 N. Charles Street,
8 Baltimore, MD 21218, USA*

9 ³*LESIA, Observatoire de Paris, Université PSL, CNRS, Sorbonne Université, Université de Paris,
10 5 place Jules Janssen, 92195 Meudon, France*

11 ⁴*IAPS-INAF, via del Fosso del Cavaliere, 100, 00133 Roma, Italy*

12 ⁵*Physikalisches Institut, University of Bern, Sidlerstrasse 5, 3012 Bern, Switzerland*

13 ⁶*Laboratory for Atmospheric and Space Physics (LASP), University of Colorado Boulder, Boulder,
14 CO 80303, USA*

15 ⁷*Institute for Modeling Plasma, Atmospheres and Cosmic Dust, NASA/SSERVI, Moffet Field, CA
16 94035, USA*

17 ⁸*LPC2E, CNRS, Université d'Orléans, 45071 Orléans, France*

18 ⁹*Southwest Research Institute, Department of Space Studies, Suite 300, 1050 Walnut Street, Boul-
19 der, CO 80302, USA*

20 ¹⁰*Swedish Institute of Space Physics, Ångström Laboratory, Lägerhyddsvägen 1, 752 37 Uppsala,
21 Sweden*

23 **Having a nucleus darker than charcoal, comets are usually detected from Earth through**
24 **the emissions from their coma. The coma is an envelope of gas which forms through the sub-**
25 **limation of ices from the nucleus, as the comet gets closer to the Sun. In the far ultraviolet,**
26 **observations of comae have revealed the presence of atomic hydrogen and oxygen emissions.**
27 **When observed over large spatial scales as seen from Earth, such emissions are dominated**
28 **by resonance fluorescence pumped by solar radiation. Here we analyse atomic emissions ac-**
29 **quired close to the cometary nucleus by the Rosetta spacecraft. In order to identify their ori-**
30 **gin, we undertake a quantitative multi-instrument analysis of these emissions by combining**
31 **coincident neutral gas, electron, and spectroscopic observations together. We establish that**
32 **the atomic emissions detected from Rosetta around comet 67P/Churyumov-Gerasimenko at**
33 **large heliocentric distances result from the dissociative excitation of cometary molecules**
34 **by accelerated solar-wind electrons (and not electrons produced from photo-ionisation of**
35 **cometary molecules as suggested in past studies). We reveal their auroral nature. Similar to**
36 **the discrete aurorae at Earth and Mars, this newly-discovered cometary aurora is driven by**
37 **the interaction of the solar wind with the local environment. We highlight how OI 1356 Å**
38 **could be used as a tracer of solar-wind electron variability.**

39 The Rosetta spacecraft escorted comet 67P/Churyumov-Gerasimenko (referred as 67P here-
40 after) for more than two years^{1,2}. Onboard, the Alice ultraviolet imaging spectrograph³ detected
41 Far UltraViolet (FUV) atomic hydrogen and oxygen emissions⁴⁻⁷ from the cometary coma. Spec-

42 troscopic analysis of these emissions shows that their origin seems to be consistent with the disso-
43 ciative excitation of cometary molecules, such as H₂O and O₂⁸, by electrons^{4,7}. The same process
44 is taking place at the Jovian moons, Ganymede^{9,10} and Europa¹¹, though the magnetic and particle
45 environments are very different. Observed from Earth over large spatial scales, the FUV atomic
46 emissions from comets primarily result from resonance fluorescence¹² (e.g., HI Ly α , HI Ly β ,
47 and OI 1304 Å) pumped by solar radiation and occurring in atoms in the extended coma. These
48 atoms are produced by photodissociation of cometary molecules by solar radiation. Observations
49 from Earth of faint OI 1356 Å emissions were reported for very active comets¹³. Such a spin
50 forbidden emission was attributed to the dissociative excitation of cometary molecules by elec-
51 trons. These electrons are expected to be photoelectrons resulting from the ionisation of cometary
52 neutrals by solar Extreme UltraViolet (EUV) radiation¹³. Similarly, the electrons thought to be
53 responsible for the excitation of FUV atomic emissions observed from Rosetta are also supposed
54 to be photoelectrons^{4,7}. This means that the FUV emissions seen close to the nucleus by Rosetta
55 are presumed to be dayglow which primarily results from the interaction of solar photons (and
56 induced photoelectrons) with an atmosphere or a coma. In contrast, auroral emissions – as defined
57 here – originate from the interaction of energetic, extra-atmospheric particles with an atmosphere
58 or, more generally, the envelope of gas surrounding a planetary body¹⁴. By “energetic”, we refer
59 to particles energetic enough to trigger the excitation which leads to emission. The energy range
60 varies with the auroral process. For dissociative excitation of water, the minimum energy required
61 for the FUV lines analysed here are between 14 and 17 eV. The planetary body does not need to
62 have an intrinsic magnetic field to host aurorae. However, to be auroral, emissions need to be driven

63 by energetic particles whose source is external (that is, not locally produced, like photoelectrons).

64 Northern and southern lights, the so-called aurora illuminating the high latitude skies on
65 Earth, have captured the human imagination for centuries. They are highly relevant for providing
66 a snapshot of the particle energy input over the high latitude regions¹⁵ and play a key role in space
67 weather. Over the past half century, auroral emissions have been discovered at planets and moons
68 in the Solar System^{14,16,17} and beyond¹⁸. Aurora is a universal phenomenon, accessible to obser-
69 vations and analysis: aurora is a tracer of plasma interaction, a remote-sensing of magnetic field
70 configuration, and a fingerprint of particle sources and atmospheric species¹⁴. So far, at comets, au-
71 roral emissions have been reported in the X-rays and EUV, resulting from the interaction of heavy
72 solar-wind ions with cometary gases^{14,19}. Here we undertake a multi-instrument analysis of FUV
73 atomic emissions (HI Ly β line and OI 1356 Å, and OI 1304 Å multiplets), by combining coincident
74 Rosetta datasets together and comparing observed and modelled brightnesses. Observations of the
75 energetic (10–200 eV) electron distribution, neutral gas (in situ and remote), and FUV emissions,
76 acquired over similar time periods at large heliocentric distances (≥ 2 AU), are linked together
77 through a physics-based model (Fig. 1). We apply this approach to nadir- and limb-viewing con-
78 figurations in order to underpin the mechanism producing the FUV atomic emissions, to identify
79 the origin of the energetic source and to reveal the nature of the emissions.

80 In order to establish the source of the FUV atomic emissions in a quantitative manner, the
81 multi-instrument analysis is applied to seven nadir-viewing cases (see Table 1). The selected cases
82 correspond to viewing over the shadowed nucleus: this avoids any contamination of the FUV

83 emissions by solar radiation reflected off the nucleus' surface⁶. We are only focusing on HI and
84 OI emissions here: the selected cases are for viewing over the northern hemisphere where water is
85 the dominant species in the coma during the periods of interest^{20,21}.

86 Comparing observed (magenta) and modelled (black) FUV brightnesses for the five 2015–
87 2016 nadir-viewing cases shows that the HI and OI emissions are produced by the dissociative
88 excitation of cometary neutrals by energetic electrons (Fig. 2). The composition (H₂O, CO₂, CO,
89 and O₂) and total column density of the neutral gas are obtained from in situ observations from the
90 Rosetta Orbiter Spectrometer for Ion and Neutral Analysis (ROSINA)²². The emission frequency is
91 derived from differential electron flux measurements from the Rosetta Plasma Consortium (RPC)²³
92 (see Extended Data Fig. 1). The neutral and electron observations combined to compute the mod-
93 elled FUV brightnesses were taken during the same time period as the FUV observations (see
94 Methods). The last three cases (26 December 2015 at 08 UT and 17 April 2016 at 11 UT and
95 22 UT) attest that in the absence of notable amounts of energetic electrons, as measured in situ
96 by the RPC electron spectrometer (see Extended Data Fig. 1 and Extended Data Fig. 2), there are
97 nearly no atomic FUV HI or OI emissions detected by the spectrograph (Fig. 2). This demon-
98 strates that there are no other significant sources contributing to the FUV atomic emissions over
99 the shadowed nucleus, beside dissociative excitation of cometary molecules by electrons. In par-
100 ticular, photodissociative excitation of cometary molecules by solar photons do not seem to play
101 any significant role here, as anticipated⁴.

102 The two 2014 cases (29 Nov at 18:00 UT, 10 Dec at 22:02 UT) correspond to a nadir pointing

103 when Rosetta was located above the neck of the bi-lobed nucleus (Table 1). Comparing observed
104 and modelled OI FUV brightnesses for these two cases, for which a pure water coma is assumed
105 in the absence of in situ gas composition measurements, shows that the observed OI FUV bright-
106 nesses are consistent with dissociative excitation of a nearly-pure water coma (Fig. 2-b). This
107 confirms earlier findings that the coma over the neck is primarily composed of water^{4,20,21}. In
108 this concave region, the outgassing is very active²¹ and emanates in many directions, enhanced by
109 self-illumination during low subsolar latitudes²⁴. It is also difficult to derive the detailed activity of
110 the surface in the neck. As a result, the water column density used as input to the model cannot be
111 straightforwardly derived from the number density measured at Rosetta (combined with a simple
112 extrapolation). It is instead set to give the modelled HI Ly β brightness in agreement (within 4%)
113 with the observed one (Fig. 2a and Table 1). The column density of $(3.8 \pm 0.8) \times 10^{15} \text{ cm}^{-2}$,
114 obtained for the 29 November 2014 case, is consistent with the value of $(4.6 \pm 0.3) \times 10^{15} \text{ cm}^{-2}$
115 derived from Visible and InfraRed Thermal Imaging Spectrometer (VIRTIS)²⁵ observations. The
116 sensitivity of the OI modelled brightnesses by adding small amounts of O₂, CO, or CO₂ to the
117 assumed pure water coma is discussed in the Methods section.

118 In order to establish the origin of the energetic electrons responsible for the FUV auroral
119 emissions, the multi-instrument analysis is applied to limb viewing. In that configuration, the FUV
120 spectrograph is staring off nadir at the cometary coma and observing FUV emissions produced
121 in a region of the coma not located between the cometary nucleus and Rosetta. By linking FUV
122 emissions from such a remote region with the emission frequency derived from in-situ electron
123 flux measurements at Rosetta, we are assessing whether energetic electrons are accelerated/heated

124 locally, or they have a large-scale external origin (e.g., hemispheric scale or more). In the former
125 case, the FUV emissions should not be correlated with the energetic electrons, while in the latter,
126 they should be. Without direct measurements of the detailed neutral composition in the remote
127 region observed, the analysis is only applied to HI Ly β which is solely driven by water. The
128 modelled brightness is derived by multiplying the water column density deduced from Microwave
129 Instrument for the Rosetta Orbiter (MIRO)²⁶ measurements and VIRTIS infrared observations (co-
130 incident with the FUV observation periods), with the HI Ly β emission frequency derived from
131 simultaneous in situ RPC electron flux measurements at Rosetta (see Methods for details). Two
132 limb-viewing intervals of two days in October 2014 have been analysed (Tables 1 and 2).

133 Past studies looked at the correlation between the limb brightness in HI Ly β from Alice
134 FUV spectrograph and the water column density from VIRTIS infrared spectrometer⁷ and at the
135 correlation between the limb brightness in OI 1356 Å from Alice and the energetic electron density
136 from RPC²⁷. In contrast, here the observed FUV brightness is quantitatively compared with the
137 modelled brightness driven by simultaneous in situ observations of the energetic electron flux from
138 RPC (taking into account the energy distribution of the electrons) and by the water column density
139 measured remotely from Rosetta.

140 Comparing the HI Ly β calculated (blue) and observed (magenta) brightnesses on 18–19 Oc-
141 tober 2014 (Fig. 3-a) and 22–23 October 2014 (Fig. 3-b) confirms that overall the prime source of
142 the HI Ly β emissions is the dissociative excitation of water. There is a good agreement in terms of
143 both magnitude and variability. The relative difference in magnitude is $30\% \pm 21\%$ over all periods

144 (13%±6% for P3) on 18–19 October 2014; it is 22%±18% over all periods (11%±10% for P3)
145 on 22–23 October 2014. The contribution from resonance scattering driven by the interplanetary
146 medium along the line of sight has been subtracted and amounts to ~1.5 Rayleigh, while the con-
147 tribution from the coma is negligible (see Methods). For a given time, the brightness averaged over
148 the rows at the centre of the slit is shown with a dot, while the vertical, light pink bar extends from
149 the brightness from rows looking closest to the nucleus (upper bound) to the brightness from rows
150 farthest away from the nucleus (lowest bound) for selected row ranges (see Table 1). The width of
151 the pink bars corresponds to the FUV observation integration time (10 min). The observed limb
152 brightnesses have a ± 30% uncertainty, shown with vertical, thin, magenta lines for three times on
153 each panel.

154 The very good agreement between the observed and modelled brightnesses in Fig. 3 attests
155 that the differential electron fluxes measured at Rosetta are consistent with those driving the FUV
156 emissions: the energetic electrons are not locally accelerated/heated. As the water column density
157 is fixed over each FUV observation period P_x (Table 2), the variations in the modelled brightness
158 during P_x is only driven by the variation in the RPC differential electron fluxes. The very good
159 correlation between the observed and modelled brightness variations includes the overall decrease
160 during P2 on 18 October 2014, the sharp intensification at 16:30 UT and the drop at 21 UT on 22
161 October 2014, and the decline over P4 on 23 October 2014. The sharp intensification at 16:30 UT,
162 seen in both the modelled and the observed brightnesses, coincides with a large increase in the
163 local plasma density and is associated with the arrival of a solar event²⁸. The mean energy and
164 number density of the energetic electrons increase suddenly, which yields an enhancement in both

165 the emission and ionisation frequencies²⁹.

166 Finally, though photoelectrons are present along the line of sight, they cannot constitute the
167 bulk of the energetic electrons responsible for the FUV emissions. The source of the energetic pop-
168 ulation must be external, as attested by the variability observed in the RPC differential electron flux
169 over the limb-viewing periods. Additional evidence is the anti-correlation between the electron-
170 impact ionisation frequency and the local outgassing rate observed away from perihelion^{29,30}.

171 The Rosetta multi-instrument analysis linking coincident particle, neutral gas, and FUV
172 emission datasets together shows that the FUV emissions over the shadowed nucleus observed
173 at large heliocentric distances are dominantly produced by the dissociative excitation of cometary
174 molecules by energetic electrons. The auroral FUV OI emissions at Ganymede^{9,10} and at Europa¹¹
175 are produced by the same type of excitation, while at Earth³¹ and Venus³² they are primarily in-
176 duced by electron impact on atomic oxygen. However, the source of the energetic electrons is
177 very different at comet 67P – subject to the interplanetary magnetic field frozen into the solar wind
178 – compared with the ones at the Galilean moons, which are embedded in the intense magnetic
179 field of Jupiter. The energetic electrons, found to be inducing the FUV emissions at comet 67P at
180 large heliocentric distances, were already found to produce most of the ionisation in the coma²⁹.
181 They are hence responsible for the presence of a cometary plasma, denser (though colder) than the
182 ambient solar wind, around the nucleus.

183 Applied to the limb viewing, the multi-instrument analysis demonstrates that the main source
184 of the energetic electrons is not local (hence not photoelectrons as originally thought^{4,7}). Based

185 on the definition proposed for auroral emissions, this reveals the auroral nature of the FUV atomic
186 emissions. We show that the source of energetic electrons involves a large-scale acceleration mech-
187 anism. This finding is consistent with a particle-in-cell simulation applied to a weakly-outgassing
188 comet³³ (Fig. 4). The self-consistent simulation shows that solar-wind electrons (red dots) undergo
189 acceleration primarily along the draped magnetic field lines when they fall into a potential well as
190 they get closer to the cometary nucleus (trajectories color-coded by the electron energy in Fig. 4).
191 This potential well is produced by an ambipolar electric field generated by the cometary plasma and
192 resulting from the large electron pressure gradient^{33,34}. This result confirms the original finding³⁵
193 that the observed differential electron fluxes are too intense and energetic to be explained by un-
194 perturbed photoelectrons or unperturbed solar-wind electrons, though they are consistent with the
195 presence of an ambipolar electric field.

196 At Earth, ambipolar electric fields (set up by electron pressure gradients between the cold,
197 dense, ionospheric plasma and the hot, tenuous, magnetospheric plasma) are at least sometimes
198 significant contributors to the large-scale, quasi-stationary, field-aligned electric fields observed
199 in the auroral (upward field-aligned current) regions³⁶. Similar to what is observed at comet 67P,
200 these large-scale electric fields observed at Earth are responsible for the electron acceleration along
201 the magnetic field lines. More generally, just like for discrete aurorae at Earth and Mars^{17,37} (which
202 result from the interaction of the terrestrial magnetosphere and the martian remanent crustal mag-
203 netic field with the solar wind), we show that the energetic electrons at comet 67P are accelerated
204 by large-scale electric fields arising from the interaction of the cometary plasma with the solar
205 wind. Lacking an intrinsic magnetic field, the cometary aurora is diffuse, while the terrestrial and

206 martian discrete aurorae are spatially confined. In contrast to the martian diffuse aurora³⁸, it occurs
207 even in the absence of solar energetic particle outbursts.

208 While aurora is a universal process, the combination of the excitation process (the same as
209 at Ganymede and Europa) and of the particle acceleration process (resulting from the interaction
210 of the solar wind with the body through electric field acceleration, similar to the discrete aurorae
211 at Earth and Mars) renders the FUV auroral emissions at comet 67P unique. The discovery of
212 the presence of cometary auroral emissions induced by solar-wind electrons at large heliocentric
213 distances offers the opportunity to use FUV emissions as a probe of the space environment at
214 a comet location: observations of OI 1356 Å (emission not affected by resonance fluorescence)
215 could be used as a proxy for solar-wind electron variability, which would be highly relevant for
216 space weather applications.

217 **References**

- 218 1. Taylor, M. G. G. T., Altobelli, N., Buratti, B. J. & Choukroun, M. The Rosetta mission orbiter
220 science overview: the comet phase. *Philos. Trans. R. Soc. A* **375**, 20160262 (2017).
- 221 2. Glassmeier, K.-H., Boehnhardt, H., Koschny, D., Kührt, E. & Richter, I. The Rosetta Mission:
222 Flying Towards the Origin of the Solar System. *Space Sci. Rev.* **128**, 1–21 (2007).
- 223 3. Stern, S. A. *et al.* Alice: The Rosetta Ultraviolet Imaging Spectrograph. *Space Sci. Rev.* **128**,
224 507–527 (2007).
- 225 4. Feldman, P. D. *et al.* Measurements of the near-nucleus coma of comet 67P/Churyumov-

- 226 Gerasimenko with the Alice far-ultraviolet spectrograph on Rosetta. *Astron. Astrophys.* **583**,
227 A8 (2015).
- 228 5. Feldman, P. D. *et al.* The Nature and Frequency of the Gas Outbursts in Comet
229 67P/Churyumov-Gerasimenko Observed by the Alice Far-ultraviolet Spectrograph on Rosetta.
230 *Astrophys. J. Lett.* **825**, L8 (2016).
- 231 6. Feldman, P. D. *et al.* FUV Spectral Signatures of Molecules and the Evolution of the Gaseous
232 Coma of Comet 67P/Churyumov-Gerasimenko. *Astron. J.* **155**, 9 (2018).
- 233 7. Chaufray, J.-Y. *et al.* Rosetta Alice/VIRTIS observations of the water vapour UV electroglow
234 emissions around comet 67P/Churyumov-Gerasimenko. *Mon. Not. R. Astron. Soc.* **469**, S416–
235 S426 (2017).
- 236 8. Bieler, A. *et al.* Abundant molecular oxygen in the coma of comet 67P/Churyumov-
237 Gerasimenko. *Nature* **526**, 678–681 (2015).
- 238 9. Feldman, P. D. *et al.* HST/STIS Ultraviolet Imaging of Polar Aurora on Ganymede. *Astrophys.*
239 *J.* **535**, 1085–1090 (2000).
- 240 10. Molyneux, P. M. *et al.* Hubble Space Telescope Observations of Variations in Ganymede’s
241 Oxygen Atmosphere and Aurora. *J. Geophys. Res. Space Phys.* **123**, 3777–3793 (2018).
- 242 11. Roth, L. *et al.* Transient Water Vapor at Europa’s South Pole. *Science* **343**, 171–174 (2014).

- 243 12. Lupu, R. E., Feldman, P. D., Weaver, H. A. & Tozzi, G.-P. The fourth positive system of
244 carbon monoxide in the Hubble Space Telescope spectra of comets. *Astrophys. J.* **670**, 1473–
245 1484 (2007).
- 246 13. Sahnou, D. J. Feldman, P. D., McCandliss, S. R. & Martinez, M.-E. Long-slit ultraviolet
247 spectroscopy of Comet Austin (1990 V). *Icarus* **101**, 71–83 (1993).
- 248 14. Galand, M. & Chakrabarti, S. Auroral Processes in the Solar System. *Washington DC Ameri-*
249 *can Geophysical Union Geophysical Monograph Series* **130**, 55 (2002).
- 250 15. Germany, G. A., *et al.* Remote determination of auroral energy characteristics during substorm
251 activity. *Geophys. Res. Lett.* **24**, 995–998 (1997).
- 252 16. Drossart, P. *et al.* Detection of H_3^+ on Jupiter. *Nature* **340**, 539–541 (1989).
- 253 17. Bertaux, J.-L. *et al.* Discovery of an aurora on Mars. *Nature* **435**, 790–794 (2005).
- 254 18. Hallinan, G. *et al.* Magnetospherically driven optical and radio aurorae at the end of the stellar
255 main sequence. *Nature* **523**, 568–571 (2015).
- 256 19. Lisse, C. M. *et al.* Discovery of X-ray and Extreme Ultraviolet Emission from Comet
257 C/Hyakutake 1996 B2. *Science* **274**, 205–209 (1996).
- 258 20. Hässig, M. *et al.* Time variability and heterogeneity in the coma of 67P/Churyumov-
259 Gerasimenko. *Science* **347**, aaa0276 (2015).

- 260 21. Migliorini, A. *et al.* Water and carbon dioxide distribution in the 67P/Churyumov-
261 Gerasimenko coma from VIRTIS-M infrared observations. *Astron. Astrophys.* **589**, A45
262 (2016).
- 263 22. Balsiger, H. *et al.* Rosina Rosetta Orbiter Spectrometer for Ion and Neutral Analysis.
264 *Space Sci. Rev.* **128**, 745–801 (2007).
- 265 23. Carr, C. *et al.* RPC: The Rosetta Plasma Consortium. *Space Sci. Rev.* **128**, 629–647 (2007).
- 266 24. Keller, H. U. *et al.* Insolation, erosion, and morphology of comet 67P/Churyumov-
267 Gerasimenko. *Astron. Astrophys.* **583**, A34 (2015).
- 268 25. Coradini, A. *et al.* VIRTIS: An Imaging Spectrometer for the Rosetta Mission. *Space Sci. Rev.*
269 **128**, 529–559 (2007).
- 270 26. Gulkis, S. *et al.* MIRO: Microwave Instrument for Rosetta Orbiter. *Space Sci. Rev.* **128**,
271 561–597 (2007).
- 272 27. Noonan, J. W. *et al.* Ultraviolet Observations of Coronal Mass Ejection Impact on Comet
273 67P/Churyumov-Gerasimenko by Rosetta Alice. *Astron. J.* **156**, 16 (2018).
- 274 28. Witasse, O. *et al.* Interplanetary coronal mass ejection observed at STEREO-A, Mars, comet
275 67P/Churyumov-Gerasimenko, Saturn, and New Horizons en route to Pluto: Comparison of
276 its Forbush decreases at 1.4, 3.1, and 9.9 AU. *J. Geophys. Res. Space Phys.* **122**, 7865–7890
277 (2017).

- 278 29. Heritier, K. L. *et al.* Plasma source and loss at comet 67P during the Rosetta mission. *Astron.*
279 *Astrophys.* **618**, A77 (2018).
- 280 30. Galand, M. *et al.* Ionospheric plasma of comet 67P probed by Rosetta at 3 au from the Sun.
281 *Mon. Not. R. Astron. Soc.* **462**, S331–S351 (2016).
- 282 31. Strickland, D. J., Daniell Jr., R. E., Jasperse, J. R. & Basu, B. Transport-theoretic model for
283 the electron-proton-hydrogen atom aurora, 2. Model results. *J. Geophys. Res. Space Phys.* **98**,
284 21,533–21,548 (1993).
- 285 32. Fox, J. L. & Stewart, A. I. F. The Venus ultraviolet aurora - A soft electron source. *J. Geo-*
286 *phys. Res.* **96**, 9821–9828 (1991).
- 287 33. Deca, J. *et al.* Building a weakly outgassing comet from a generalized ohm's law. *Phys. Rev.*
288 *Lett.* **123**, 055101 (2019).
- 289 34. Divin, A. *et al.* A Fully Kinetic Perspective of Electron Acceleration around a Weakly Out-
290 gassing Comet. *Astrophys. J. Lett.* **889**, L33 (2020).
- 291 35. Madanian, H. *et al.* Suprathermal electrons near the nucleus of comet 67P/Churyumov-
292 Gerasimenko at 3 AU: Model comparisons with Rosetta data. *J. Geophys. Res. Space Phys.*
293 **121**, 5815–5836 (2016).
- 294 36. Hull, A. J., Bonnell, J. W., Mozer, F. S., Scudder, J. D. & Chaston, C. C. Large parallel electric
295 fields in the upward current region of the aurora: Evidence for ambipolar effects. *J. Geophys.*
296 *Res. Space Phys.* **108**, 1265 (2003).

- 297 37. Lundin, R. *et al.* Plasma acceleration above martian magnetic anomalies. *Science* **311**, 980–
298 983 (2006).
- 299 38. Schneider, N. M. *et al.* Discovery of diffuse aurora on Mars. *Science* **350**, 0313 (2015).
- 300 39. Jorda, L. *et al.* The global shape, density and rotation of Comet 67P/Churyumov-Gerasimenko
301 from preperihelion Rosetta/OSIRIS observations. *Icarus* **277**, 257–278 (2016).
- 302 40. Burch, J. L. *et al.* RPC-IES: The Ion and Electron Sensor of the Rosetta Plasma Consortium.
303 *Space Sci. Rev.* **128**, 697–712 (2007).
- 304 41. Markidis, S., Lapenta, G., & Rizwan-uddin Multi-scale simulations of plasma with iPIC3D.
305 *Math. Comput. Simu.* **80**, 1509–1519 (2010).
- 306 42. Makarov, O. P. *et al.* Kinetic energy distributions and line profile measurements of dissociation
307 products of water upon electron impact. *J. Geophys. Res. Space Phys.* **109**, A09303 (2004).
- 308 43. Mumma, M. J., Stone, E. J., Borst, W. L. & Zipf, E. C. Dissociative Excitation of Vacuum Ul-
309 traviolet Emission Features by Electron Impact on Molecular Gases. III. CO₂. *J. Chem. Phys.*
310 **57**, 68–75 (1972).
- 311 44. Ajello, J. M. Emission Cross Sections of CO by Electron Impact in the Interval 1260-5000 Å.
312 I. *J. Chem. Phys.* **55**, 3158–3168 (1971).
- 313 45. Kanik, I. *et al.* Electron impact dissociative excitation of O₂: 2. Absolute emission cross
314 sections of the OI(130.4 nm) and OI(135.6 nm) lines. *J. Geophys. Res. Planets* **108**, 5126
315 (2003).

- 316 46. Heritier, K. L. Cometary ionosphere analysis from Rosetta multi-instrument dataset. *PhD*
317 *Thesis Imperial College London (UK)* (2018). <https://doi.org/10.25560/66101>.
- 318 47. Odelstad, E. *et al.* Measurements of the electrostatic potential of Rosetta at comet 67P. *Mon.*
319 *Not. R. Astron. Soc.* **469**, S568–S581 (2017).
- 320 48. Eriksson, A. I. *et al.* RPC-LAP: The Rosetta Langmuir Probe Instrument. *Space Sci. Rev.* **128**,
321 729–744 (2007).
- 322 49. Edberg, N. J. T. *et al.* Solar wind interaction with comet 67P: Impacts of corotating interaction
323 regions. *J. Geophys. Res. Space Phys.* **121**, 949–965 (2016).
- 324 50. Le Roy, L. *et al.* Inventory of the volatiles on comet 67P/Churyumov-Gerasimenko from
325 Rosetta/ROSINA. *Astron. Astrophys.* **583**, A1 (2015).
- 326 51. Gasc, S. *et al.* Sensitivity and fragmentation calibration of the time-of-flight mass spectrometer
327 RTOF on board ESA’s Rosetta mission. *Planet. Space Sci.* **135**, 64–73 (2017).
- 328 52. Bockelée-Morvan, D. *et al.* First observations of H₂O and CO₂ vapor in comet
329 67P/Churyumov-Gerasimenko made by VIRTIS onboard Rosetta. *Astron. Astrophys.* **583**,
330 A6 (2015).
- 331 53. Dhiri, V. J. F., Vallat, C. & Kueppers, M. Rosetta: Payload boresight alignment details. *ESA*
332 **2**, 1–11, doi: RO–EST–TN–3305 (2014).
- 333 54. Fougere, N. *et al.* Direct Simulation Monte Carlo modelling of the major species in the coma
334 of comet 67P/Churyumov-Gerasimenko. *Mon. Not. R. Astron. Soc.* **462**, S156–S169 (2016).

- 335 55. Biver, N. *et al.* Long-term monitoring of the outgassing and composition of comet
336 67P/Churyumov-Gerasimenko with the Rosetta/MIRO instrument. *Astron. Astrophys.* **630**,
337 A19 (2019).
- 338 56. Fink, U. *et al.* Investigation into the disparate origin of CO₂ and H₂O outgassing for Comet
339 67P. *Icarus* **277**, 78–97 (2016).
- 340 57. Deca, J. *et al.* Electron and Ion Dynamics of the Solar Wind Interaction with a Weakly Out-
341 gassing Comet. *Physical Review Letters* **118**, 205101 (2017).

342 **Acknowledgements** Rosetta is a European Space Agency (ESA) mission with contributions from its mem-
343 ber states and the National Aeronautics and Space Administration (NASA). We acknowledge the continuous
344 support of the Rosetta teams at the European Space Operations Centre in Darmstadt and at the European
345 Space Astronomy Centre. We acknowledge the staff of CDDP and Imperial College for the use of AMDA
346 and the RPC Quicklook database. This work has benefited from discussions within International Team 402:
347 Plasma Environment of Comet 67P after Rosetta at the International Space Science Institute (ISSI) (Bern,
348 Switzerland). We warmly thank Nicolas Fougere for his efficient help and valuable advice using the ICES
349 models. We are very grateful to Matt Taylor for his constructive feedback. Work at Imperial College London
350 was supported by STFC of UK under grants ST/N000692/1 and ST/S505432/1, by Imperial College London
351 through a President’s Scholarship, and by ESA under contract No.4000119035/16/ES/JD. The Alice team
352 acknowledges support from NASA’s Jet Propulsion Laboratory through contract 1336850 to the Southwest
353 Research Institute. M. R. acknowledges the support of the State of Bern and the Swiss National Science
354 Foundation (200021_165869, 200020_182418). J. D. gratefully acknowledges support from NASAs Rosetta
355 Data Analysis Program, Grant No. 80NSSC19K1305, NASA’s Solar System Exploration Research Virtual

356 Institute (SSERVI): Institute for Modeling Plasmas, Atmosphere, and Cosmic Dust (IMPACT), and the com-
357 putational resources provided by the NASA High-End Computing (HEC) Program through the NASA Ad-
358 vanced Supercomputing (NAS) Division at Ames Research Center. We acknowledge PRACE for awarding
359 us access to Curie at GENCI@CEA, France. Work at LPC2E/CNRS was supported by CNES and by ANR
360 under the financial agreement ANR-15-CE31-0009-01. VIRTIS was built by a consortium, which includes
361 Italy, France, and Germany, under the scientific responsibility of the Istituto di Astrofisica e Planetologia
362 Spaziali of INAF, Italy, which also guides the scientific operations. The VIRTIS instrument development,
363 led by the prime contractor Leonardo-Finmeccanica (Florence, Italy), has been funded and managed by ASI,
364 with contributions from Observatoire de Meudon financed by CNES, and from DLR. The VIRTIS calibrated
365 data will be available through the ESAs Planetary Science Archive (PSA) Website (www.rssd.esa.int) and is
366 available upon request until posted to the archive. We thank the following institutions and agencies for sup-
367 port of this work: Italian Space Agency (ASI, Italy) contract number I/024/12/1, Centre National d'Etudes
368 Spatiales (CNES, France), DLR (Germany), NASA (USA) Rosetta Program, and Science and Technology
369 Facilities Council (UK). All ROSINA data are the work of the international ROSINA team (scientists, en-
370 gineers and technicians from Switzerland, France, Germany, Belgium and the US) over the past 25 years,
371 which we herewith gratefully acknowledge.

372 **Author contributions** M.G. led the study, performed the multi-instrument analysis, generated Fig. 2 and
373 Fig. 3, and wrote the manuscript. P.D.F. identified times of interest for Alice, analysed the FUV dataset,
374 advised on the different emission source mechanisms, and estimated the interplanetary medium contribution.
375 D.B.-M. and Y.-C.C. analysed the VIRTIS-H dataset. N.B. analysed the MIRO dataset. G.R. analysed the
376 VIRTIS-M dataset. M.R. and K.A. (Principal investigator of the ROSINA instrument) provided the ROSINA
377 dataset. They all provided guidance on the interpretation of their respective dataset. J.D. generated Fig. 4

378 based on the output of a PiC simulation he ran. J.D. and P.H. provided guidance on the PiC simulation
379 interpretation. A.B., P.S. and K.L.H. provided feedback on the multi-instrument analysis. A.B. generated
380 Fig. 1. J.Wm.P. (Principal investigator of the Alice instrument) contributed to the interpretation of the Alice
381 dataset. C.C., A.I.E., and J.B. (all Principal investigators of RPC) provided guidance on the interpretation
382 of the RPC dataset. A.I.E. provided the RPC-LAP dataset. All authors contributed to the interpretation of
383 the results and commented on this manuscript.

384 **Interest declaration** The authors declare that they have no competing financial interests.

385 **Correspondence** Correspondence and requests for materials should be addressed to M. Galand (email:
386 mgaland@ic.ac.uk).

387 **Methods**

388 We apply a multi-instrument analysis linking coincident Rosetta electron, neutral gas, and FUV emission
389 observations together (Fig. 1). The measured FUV brightnesses for HI and OI emissions are compared with
390 the calculated brightnesses derived from electron and neutral gas measurements. The latter includes in situ
391 measurements from a mass spectrometer as well as remote-sensing sub-mm and infrared observations. The
392 auroral nature that we derive for the FUV emissions is consistent with a particle-in-cell simulation applied
393 to low outgassing comets.

394 **Modelled FUV brightnesses.** We calculate the brightness of three atomic emissions, HI Ly β line (1026 Å)
395 and OI multiplets (1304 Å and 1356 Å), for seven cases in nadir viewing over the shadowed nucleus and for
396 two periods of two days in limb viewing (Table 1). The number of cases is restricted by the requirements
397 (1) to have analysed FUV brightness observations, with high enough signal to noise, over the northern

398 hemisphere, (2) for the nadir study, to have the FUV spectrograph viewing along the nadir over the shadowed
 399 nucleus and to have simultaneous in situ neutral density and composition measurements (though two cases
 400 without neutral composition were included as they were over the nucleus' neck where the coma is known
 401 to be almost pure water), (3) for the limb study, to have coincident limb-viewing observations from the
 402 FUV spectrograph and from either the sub-mm instrument or one of the infrared sensors. The brightness
 403 (in Rayleigh) of an atomic emission X is assumed to be produced by the dissociative excitation of neutral
 404 molecules by energetic electrons. It is assessed, as a function of the time t , as follows:

$$B^X(t) = 10^{-6} \nu^X(t) C(t) \quad (1)$$

405 where ν^X is the combined frequency (in s^{-1}) of dissociative excitation of neutral cometary species which
 406 contribute to the production of the atomic emission X and C is the total column density (in cm^{-2}), along the
 407 line of sight, of these neutral species. As HI Ly β is only produced by the dissociation of water, its brightness
 408 is derived from the emission frequency of water and the water column density along the line of sight. As
 409 the OI emissions are induced by the dissociation of several neutral species, their brightnesses are calculated
 410 from the combined emission frequency (defined hereafter) and the total column density of H₂O, CO₂, CO,
 411 and O₂ along the line of sight. For the nadir viewing, the modelled value provided for each case derives
 412 from the average value over all measurements of RPC-Ion and Electron Sensor (IES)⁴⁰ over the observing
 413 time of Alice (Fig. 2 and Table 1). For the limb viewing, the modelled values are provided at each time that
 414 an energetic electron spectrum of RPC-IES is measured (Fig. 3). The typical time resolution of RPC-IES
 415 over the selected limb-viewing days is 4 min.

416 *Electron-impact emission frequency:* The emission frequency ν_n^X of the atomic emission X (HI Ly β ,
 417 OI 1304, OI 1356) associated with the dissociation of the neutral species n (H₂O, O₂, CO₂, CO) is cal-

418 culated at time t at the location of Rosetta as follows:

$$\nu_n^X(t) = \int_{E_n^X}^{E_{max}} \sigma_n^X(E) J_e(t, E) dE \quad (2)$$

419 where $\sigma_n^X(E)$ is the dissociative excitation cross section (in cm^2) of n by an electron of energy E and
420 $J_e(t, E)$ is the differential electron flux (in $\text{cm}^{-2} \text{s}^{-1} \text{eV}^{-1}$) measured at time t . We consider cross sections
421 from H_2O yielding HI Ly β and OI emissions⁴², from CO_2 yielding OI 1304⁴³ and OI 1356⁴, from CO
422 yielding OI multiplets⁴⁴, and from O_2 yielding OI multiplets⁴⁵. J_e can be assumed to be constant along the
423 line of sight^{7,29}. It is obtained from the electron intensity (in $\text{cm}^{-2} \text{s}^{-1} \text{eV}^{-1} \text{sr}^{-1}$) measured by the RPC–
424 IES spectrometer, after integrating the intensity over elevation and azimuthal angles and assuming isotropy
425 for blind spots due to obstruction or the limited field of view⁴⁶. The differential electron flux is also corrected
426 for the spacecraft potential⁴⁷ – obtained from RPC–LAP⁴⁸ – by applying Liouville’s theorem³⁰. For the 10
427 December 2014 case, as no data is available for the spacecraft potential V_{sc} , it is set to -10 V. The arrival
428 of a CIR on 22 October 2014 at 16:30 UT rendered the spacecraft potential very negative but could not be
429 derived from RPC–LAP over the rest of the day and the next day until 06 UT⁴⁹. From 16:30 UT onward
430 on 22 October 2014, V_{sc} is set to -25 V (part of P1 and the full period, P2), while on 23 October 2014
431 which was less disturbed, it is set to -15 V (periods P3 and P4). The RPC–IES dataset is not reliable after
432 17:25 UT on 22 October 2014 for about 15-20 min, so it is disregarded. The energy E_{max} is the maximum
433 energy considered which is set to 200 eV; beyond this value, the signal is primarily at the background level.
434 We have checked that the emission frequency is not sensitive to the choice of a higher value for E_{max} , testing
435 it up to 400 eV. The energy E_n^X represents the energy threshold of the dissociative excitation process; its
436 value is 17 eV for HI Ly β from the dissociation of H_2O ; it varies between 14-15 eV (H_2 , O_2) to 20-21 eV
437 (CO , CO_2) for the OI emissions. When V_{sc} is very negative, the corrected differential electron flux from
438 RPC–IES starts at an energy E_{min} above the ionisation threshold. In that case, it is extrapolated towards
439 lower energies assuming a constant value equal to the measured value at E_{min} . Two examples of differential

440 electron fluxes, measured by the RPC–IES electron spectrometer and used in the nadir study, are presented
 441 in the Extended Data Fig. 1. One was taken at 11:47 UT (orange crosses) during the FUV observation
 442 period on 29 March 2015 starting at 11:43 UT and the other, at 08:35 UT (red pluses) taken during the FUV
 443 observation period on 26 December 2015 (Table 1). The differential fluxes are corrected for the spacecraft
 444 potential; as, by coincidence, the latter is of the same order in both cases (-2 V), the spectra start at about the
 445 same energy (8.3–8.4 eV). By integration, the density of electrons with energies between 10 eV and 200 eV
 446 is derived and found to be 30 times higher in the March case than in the December case (see Extended Data
 447 Fig. 2). The former is associated with a period when significant FUV emissions are detected, while the latter
 448 is associated with a period of absence of significant FUV emissions (see Figure 2). For these two cases, the
 449 total column density of neutral gas, C^{COPS} , is similar (see Extended Data Fig. 2).

450 Unlike HI $\text{Ly}\beta$ which is only induced by the dissociation of water, OI emissions are produced by the dis-
 451 sociative excitation of all four major species. In that case, it is necessary to assess an effective emission
 452 frequency, defined as:

$$\nu^X(t) = \sum_n v_n(t) \nu_n^X(t) \quad (3)$$

453 where $v_n(t)$ is the volume mixing ratio of the neutral species n at time t . It is derived from the analysis of
 454 the ROSINA–DFMS dataset obtained during the observing period of the Alice FUV spectrograph. The data
 455 processing and analysis of ROSINA-DFMS to derive the neutral composition are described in Le Roy et
 456 al.⁵⁰. The neutral composition is assumed to be constant in the nadir-viewing column of the coma. When it
 457 is not available (e.g., 2014 nadir-viewing cases), the forward modelling is performed for a pure-water coma.
 458 The closest DFMS measurements to one of the 2014 nadir-viewing cases was made on 10 December 2014
 459 at 22 UT. It shows that, after water, O₂ was the second most abundant species (3%), followed by CO (2%)
 460 and CO₂ (0.7%) with a decreasing trend (with respect to water) observed from 20 UT to 22 UT. This trend

461 suggests that the mixing ratios of the minor species during the Alice observation window (22:02–23:13 UT)
 462 are likely to be smaller than those listed above. The modelled OI brightnesses for pure water are shown
 463 in Fig. 2b. For the 10 December 2014 case, while the OI 1304 brightnesses agree within the uncertainty,
 464 the modelled OI 1356 brightness is $\sim 45\%$ lower compared with the observed brightness (which has an
 465 absolute calibration uncertainty of $\pm 20\%$). Adding 0.5% of O₂ (relative to water) brings the modelled OI
 466 brightness within 5% of the observed OI 1356 brightness (electron impact on O₂ being efficient to produce
 467 OI 1356⁴⁵), without affecting significantly the OI 1304 modelled brightness (which remains within $\sim 15\%$
 468 of the observed brightness), as OI 1304 is dominantly produced through the dissociation of water⁴². Adding
 469 2% of CO (or 1% of CO₂) to the H₂O–O₂ coma, the OI 1356 modelled brightness is higher compared
 470 with the observed brightness by 3–9% (12–16%), respectively, but remains within the uncertainties of the
 471 observed value.

472 *Nadir column density:* For nadir viewing, the total neutral column density along the line of sight corresponds
 473 to the number of molecules per unit area in the column between the Rosetta spacecraft and the surface of
 474 the nucleus. By default, the column density is derived from the total neutral density $n_{tot}^{COPS}(t, r)$ measured
 475 at time t at the Rosetta cometocentric distance r_R , by the ROSINA–Comet Pressure Sensor (COPS)²²,
 476 after correction⁵¹ for neutral composition inferred from ROSINA–DFMS. We assume a r^{-2} –dependence in
 477 cometocentric distance r for the number density down to the surface, as justified by observations^{8,20}. This
 478 means that for nadir viewing, the column density at time t is:

$$C^{COPS}(t) = n_{tot}^{COPS}(t, r_R) \frac{(r_R - r_S) r_R}{r_S} \quad (4)$$

479 where r_S is the cometocentric distance of the nucleus' surface, assumed here to be a mean value of 1.7 km³⁹.
 480 Values derived for the column density are given in Table 1 for the four 2015–2016 nadir cases and in the
 481 Extended Data Fig. 2 for the two times selected in the Extended Data Fig. 1.

482 For the two 2014 nadir cases, which correspond to cases above the highly active neck of the bi-lobed
483 nucleus³⁹, the geometry of the surface means that the gas is emitted in many directions with enhanced level
484 due to self-illumination²⁴. It is not realistic to infer the column density close to the nucleus from measure-
485 ments of the neutral density at Rosetta. Instead, the water column density is derived from the comparison
486 between the observed and modelled HI Ly β brightnesses (Table 1).

487 *Nadir column density on 29 November 2014:* Based on the HI Ly β analysis, we derive a value of $(3.8 \pm$
488 $0.8) \times 10^{15} \text{ cm}^{-2}$ (uncertainty linked to the 20% uncertainty in the observed nadir HI Ly β brightness) for
489 the water column density for the 29 November 2014 case and used it to drive the model. This value is
490 consistent with the water column density value of $(4.6 \pm 0.3) \times 10^{15} \text{ cm}^{-2}$ obtained from the high spectral-
491 resolution single-aperture spectrometer, VIRTIS-H⁵² (H for High spectral resolution) during the Alice FUV
492 observation period on the same day. It should be noted that there may be a slight difference in the close-up
493 regions seen by Alice and VIRTIS-H at such a small distance from the nucleus, as highlighted by comparing
494 their boresights and fields of view⁵³: Alice FUV brightness is from bins 15–17 along the slit (Table 1), while
495 VIRTIS-H aperture is closest to the bin 14/15 junction; the field of view of VIRTIS-H ($0.03^\circ \times 0.1^\circ$)⁵² is
496 slightly smaller than that associated with a bin of Alice ($0.05^\circ \times 0.3^\circ$)⁶. There is a slight difference in the
497 time period of the two observation sets: 17:57–18:22 UT (VIRTIS-H), 18:00–18:40 UT (Alice). The derived
498 value for the water column density is also close to the value of $6 \times 10^{15} \text{ cm}^{-2}$ deduced from the DSMC model
499 for the region of interest⁵⁴. As expected over the neck region, the water column density extrapolated from
500 the neutral density measurements at Rosetta from ROSINA and assuming a mean cometocentric distance of
501 the nucleus' surface of 1.7 km³⁹ is significantly smaller than the one deduced from VIRTIS-H (by 84%)
502 and the one derived from HI Ly β (82%).

503 *Limb column density:* For limb viewing, the column to consider along the viewing direction stretches from

504 the Rosetta spacecraft to infinity. In practice, it extends up to where the coma is dense enough to emit signif-
505 icant emissions to be detected by the remote-sensing instruments. Only HI Ly β , induced by the dissociation
506 of water, is analysed for limb cases. The water column density is derived from the Rosetta sub-mm MIRO
507 instrument and from the IR VIRTIS instrument suite. Microwave emissions at wavelengths near 0.53 mm
508 emitted by H₂¹⁸O and observed by the high spectral-resolution spectrograph from MIRO²⁶ were analysed
509 in order to derive the water column density⁵⁵. An expansion velocity of 0.68 km s⁻¹ was assumed for the
510 analysis of the limb observations. The ν_3 vibrational band of water near 2.7 μm , the strongest vibrational
511 band observed in cometary infrared spectra, was detected by VIRTIS²⁵. Emission intensities from the high
512 spectral-resolution single-aperture spectrometer, VIRTIS-H, were analysed in the 2.61–2.73 μm range in
513 order to derive water column density. The data processing and analysis of such a dataset are described in
514 Bockelée-Morvan et al.⁵². Emission intensities from the infrared channel of the medium-resolution imaging
515 spectrometer, VIRTIS-M (M for Mapper), were analysed by integrating over the 2.6–2.8 μm band after
516 subtracting the background continuum^{21,56}.

517 The water column density values used for calculating the FUV HI Ly β brightnesses during each limb-
518 viewing period (C^{limb}) are listed in the fourth column in Table 2 along with the values observed by the
519 MIRO spectrograph in the sub-mm (C^{MIRO}), by the VIRTIS IR high-resolution single-aperture spectrometer
520 ($C^{VIRTIS-H}$) and by the VIRTIS IR medium-resolution imaging spectrometer ($C^{VIRTIS-M}$). For period P3 of
521 Alice observations (around midnight on 18 October 2014), measurements from all three remote sensors are
522 available and agree very well. For the other periods, when available the water column densities derived
523 from the IR medium-resolution imaging spectrometer are consistent with those derived from the sub-mm
524 observations. As the water column density derived from the sub-mm instrument has the lowest uncertainty,
525 we set the value used for the limb-viewing calculation to its mean value.

526 **Observed FUV brightnesses.** The FUV brightnesses are derived from the Alice imaging spectrograph³ for
527 nadir and limb-staring viewings. Among HI lines, Ly β is preferable to the stronger Ly α for the present study
528 due to the complexity of instrumental effects for Alice measurements. For limb viewing, the signal is also
529 affected by the resonance scattering of the interplanetary H Lyman series, which is at least 300 times brighter
530 in HI Ly α than in HI Ly β . Even for nadir viewing over the shadowed nucleus, where such a contribution
531 is not significant, the Ly α sensitivity varies by a factor of 2 along the slit due to the uneven photocathode
532 deposited on the microchannel plate detector in the region of Ly α ³.

533 For each bin along the slit, an individual spectrum is obtained after a time integration of typically 10 min.
534 The slit has a dog-bone shape with a narrow, central region of width 0.05° and of length 2°³, spanning from
535 bins 12 to 18 (0.3°/bin). The brightnesses for nadir viewing and the main brightnesses for limb viewing
536 (magenta dots in Figure 3) are obtained from the central part of the narrow region of the slit, which provides
537 the best spectral resolution possible with Alice. The central bin of the narrow region of the slit, bin 15,
538 represents the closest bin to nadir when the z axis is nadir. All nadir viewing brightnesses are associated
539 with a bin range including bin 15 (see Table 1). The only exception is 26 December 2015 which is slightly
540 off nadir and, to a lesser extent, 17 April 2016. For limb viewing, beside the brightness around the slit's
541 centre, two other brightnesses are given at each time, one generated from bins closer to the nucleus and
542 another one from bins further away from the nucleus (Table 1).

543 Once the spectra are co-added over the bin range and the count rate converted into a value in photons·R⁻¹,
544 the spectra are sometimes averaged over time in order to improve the signal-to-noise ratio. This is done for
545 the nadir observations over the shadowed nucleus. This explains why the observing periods, which are the
546 sum of individual exposures, are ranging from 20 min to over 1 h 30 min (Table 1). For the limb viewing,
547 the original 10-min integration is conserved. After removal of the background derived from spectral regions

548 cleared of strong lines, the brightness is estimated from integration over the atomic emission.

549 The HI and OI brightnesses for two nadir-viewing cases (29 November 2014 at 18:00 UT and 29 March 2015
550 at 11:43 UT) has already been published⁶ and further information on the Alice data analysis can be found
551 there. The HI Ly β brightnesses for the two limb-viewing cases (18–19 October 2014 and 22–23 October
552 2014) are updated from Figs. 4 and 5 of Feldman et al.⁴, as since the publication the instrument calibra-
553 tion has been revised. The contribution of resonance scattering from the coma and from the interplanetary
554 medium (IPM) is estimated along the line of sight for these two observation periods. The contribution
555 from the coma is assessed to be of the order of mR assuming a spherically symmetric neutral coma: it
556 can be reliably neglected. The contribution from interplanetary HI is estimated based on nearly concur-
557 rent measurements made at larger off-nadir angles (and during a period of low measured electron flux).
558 The uncertainty on the Alice limb brightnesses, including calibration uncertainty and IPM contribution, is
559 estimated to be $\pm 30\%$.

560 **Particle-in-cell simulations.** To illustrate the large-scale energisation of electrons, we present the results
561 of a 3D fully kinetic particle-in-cell simulation applied to a weakly-outgassing comet at large heliocentric
562 distances⁵⁷. The plasma environment is simulated for an heliocentric distance of 4 AU and an outgassing
563 rate of 10^{25} s^{-1} for the cometary nucleus³³. The simulation shows that the solar-wind electrons, originally
564 at $\sim 10 \text{ eV}$, are accelerated towards the nucleus as they fall into the potential well produced by an ambipolar
565 electric field. This electric field is set up by the cometary plasma and is triggered by a strong electron
566 pressure gradient (Fig. 4).

567 **Data Availability:** The Rosetta data that support the plots within this paper and other findings of this study
568 are available from the ESA–PSA archive (<https://www.cosmos.esa.int/web/psa/rosetta>) or the NASA PDS
569 archive (https://pdssbn.astro.umd.edu/data_sb/missions/rosetta/index.shtml)

570 **Code Availability:** iPIC3D is publicly available on GitHub (<https://github.com/iPIC3D/iPIC3D>; Apache
571 License 2.0).

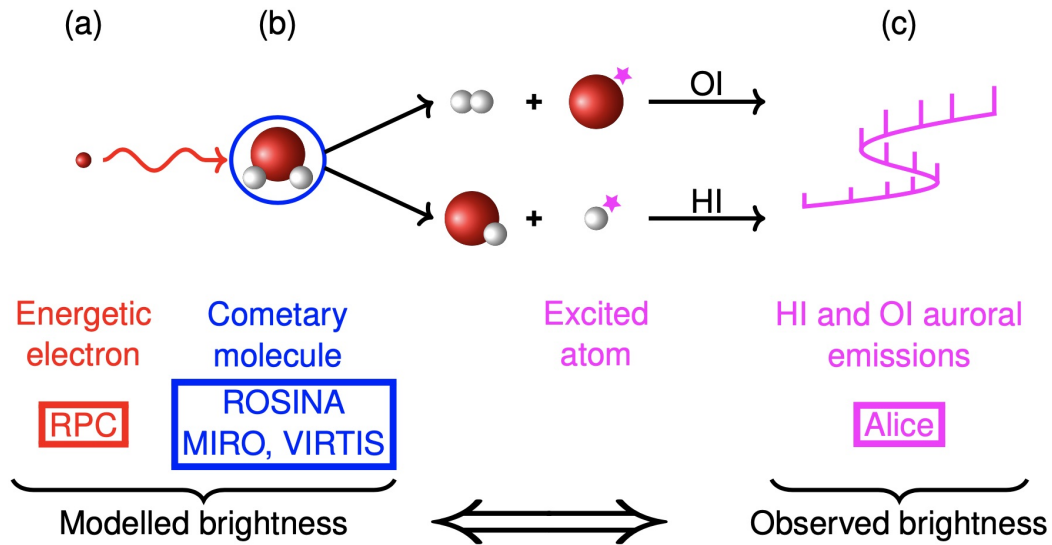


Figure 1: **Multi-instrument approach applied to analyse FUV atomic emissions.** Overview of the generation of auroral emissions through the dissociative excitation of cometary molecules by energetic (10–200 eV) electrons. A multi-instrument approach is applied to confirm the origin of the FUV emissions by linking (a) the energetic electrons measured in situ by the Rosetta Plasma Consortium (RPC)²³ electron spectrometer⁴⁰, (b) the cometary molecules observed in situ by the Rosetta Orbiter Spectrometer for Ion and Neutral Analysis (ROSINA)²² and remotely by the Microwave Instrument for the Rosetta Orbiter (MIRO)²⁶, and the Visible and InfraRed Thermal Imaging Spectrometer (VIRTIS)²⁵, and (c) the FUV atomic emissions detected by the Alice FUV spectrograph³.

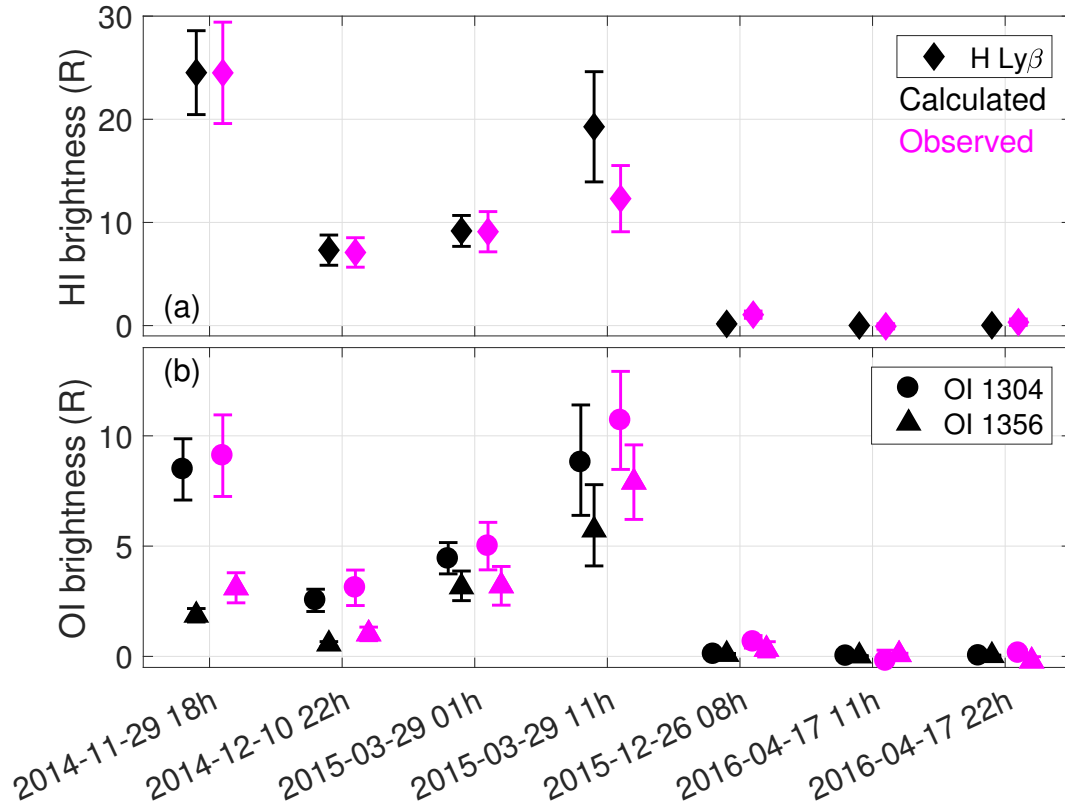


Figure 2: **Nadir-viewing analysed cases.** Nadir-viewing FUV brightnesses observed (magenta) and calculated (black) from a combination of coincident neutral gas and electron measurements (a) for HI Ly β line and (b) for OI 1304 \AA (filled circles) and OI 1356 \AA (filled triangles) multiplets. The magenta vertical bars include 20% uncertainty in the observed brightness values and $\pm 1\sigma$ standard deviation resulting from the spread over the spatial rows in the extracted spectrum. The black vertical bars represent the variability in Rosetta in situ electron fluxes over the FUV observing time combined, for the OI brightnesses, with 20% in Rosetta in situ neutral composition uncertainty (except for the 2014 cases for which a pure water coma is assumed over the neck in the absence of coincident neutral composition observations). Measured and modelled points for a given date/time are offset for visibility.

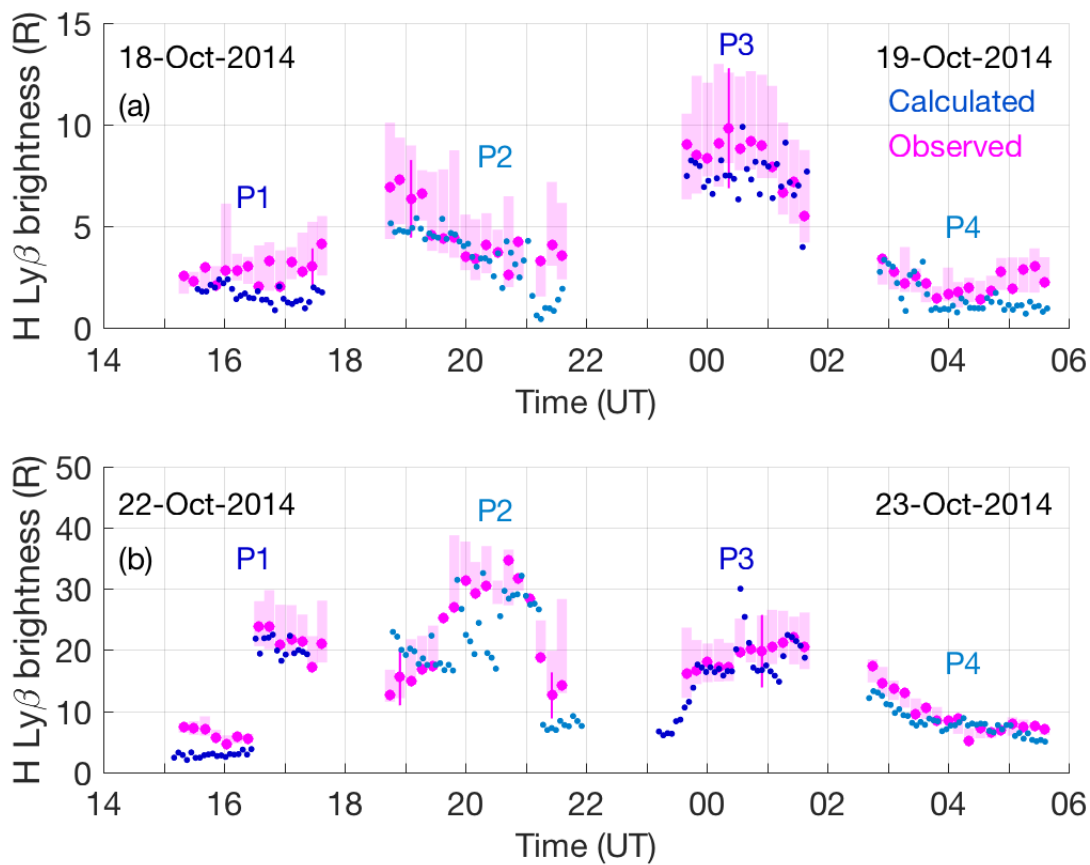


Figure 3: **Limb-viewing analysed cases.** Time series of limb-viewing observed (magenta) and calculated (blue) HI Ly β brightnesses (a) on 18–19 October 2014 and (b) on 22–23 October 2014. The model is driven by Rosetta in situ electron measurements and by the water column density derived from Rosetta remote-sensing sub-mm and IR observations (see Table 2). The observed FUV brightness is averaged over the rows at the centre of the slit (dot) and its uncertainty is $\pm 30\%$ (vertical, thin, magenta lines for three times on each panel). The vertical, light pink bar shows the variation along the slit; its width corresponds to the FUV spectrograph integration time (10 min).

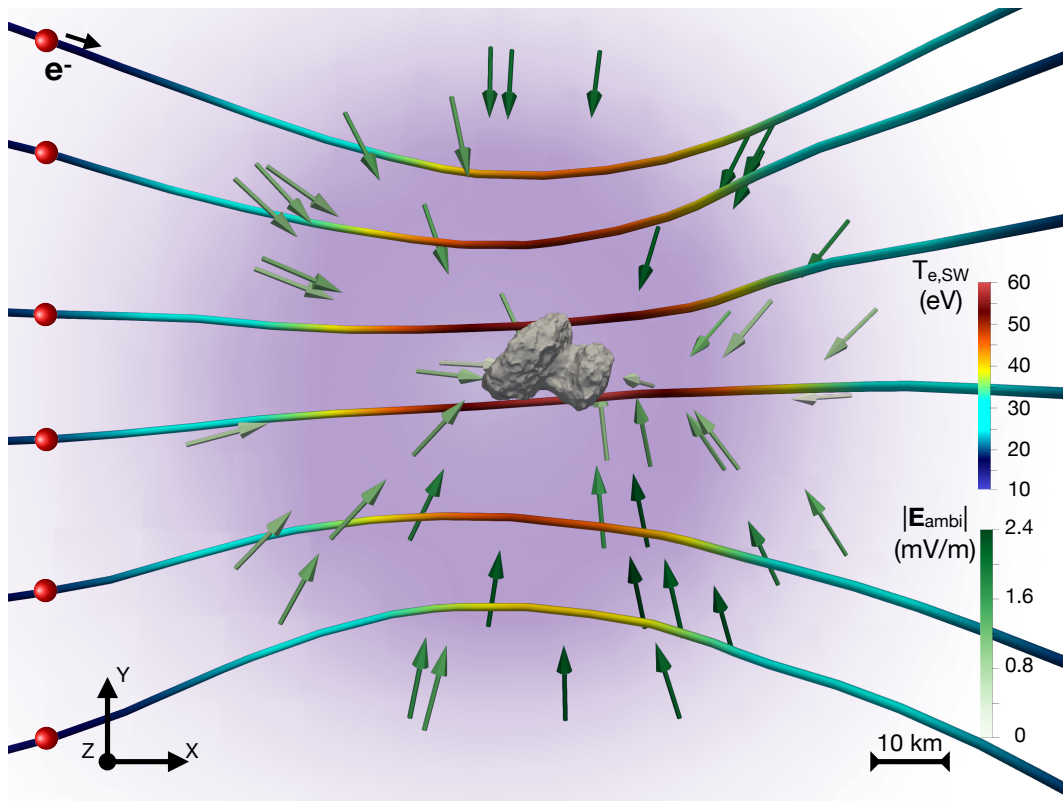


Figure 4: **Source of the energetic electrons responsible for the FUV emissions.** Trajectories of solar-wind electrons inducing the FUV aurora around comet 67P. They undergo acceleration through the ambipolar electric field set up by the cometary plasma. The electron trajectories are shown with lines colour-coded by energy and the ambipolar electric field acting on electrons ($-\mathbf{E}_{ambi}$) is plotted with green arrows. They are output from a 3D fully kinetic particle-in-cell iPIC3D⁴¹ simulation applied to a weakly-outgassing comet³³. The upstream solar wind flows along +X (towards the right), the upstream interplanetary magnetic field points along +Y (upward), and Z is complementing the orthogonal coordinate system (out of the plane). The nucleus is not to scale.

Table 1: Details on the analysed cases. For nadir viewing, are given: selected day, Alice FUV spectrograph observation start time t_0 and duration Δt (sum of all integration times used), bin number range used along the FUV spectrograph slit, heliocentric distance r_h , Rosetta cometocentric distance r_R and sub-spacecraft latitude at t_0 , and column density C between Rosetta and the nucleus' surface. For limb viewing, are given: selected day, range of bins along the FUV spectrograph slit from closest to the nucleus, centre of the slit, to furthest from the nucleus, distances r_h and r_R , FUV spectrograph off-nadir viewing angle, and integration time Δt .

Nadir viewing against the shadowed nucleus							
Selected day	t_0	Δt	Bin #	r_h	r_R	Lat.	C
	(UT)	(hh:mm)	range ^a	(AU)	(km)	(°)	(10 ¹⁵ cm ⁻²)
29 Nov 2014	18:00:01	00:40	15–17	2.87	30	51	3.8 ^b
10 Dec 2014	22:02:29	01:11	13–16	2.80	20	36	3.5 ^b
29 Mar 2015	01:04:00	00:20	13–14	1.99	43.1	14	3.5±0.1 ^c
29 Mar 2015	11:43:43	00:20	14–15	1.99	92	7	7.0±1.1 ^c
26 Dec 2015	08:05:16	01:11	09–12	1.98	79	28	4.5±0.5 ^c
17 Apr 2016	11:11:00	01:37	12–14	2.82	63	80	0.23±0.02 ^c
17 Apr 2016	22:28:00	01:17	12–14	2.82	54	82	0.26±0.02 ^c
Limb viewing							
Selected days	Bin #	Bin #	Bin #	r_h	r_R	off nadir	Δt
	closest	centre	furthest	(AU)	(km)	(°)	(min)
18-19 Oct 2014	8–12	13–17	18–22	3.16–3.15	10	15	10
22-23 Oct 2014	8–12	13–17	18–22	3.13–3.12	10	17	10

^a The centre of the slit, closest to nadir, is bin 15. ^b The total column density is deduced from HI Ly β observations

assuming a water pure coma (see text). ^c The total column density is derived from the total number density n_{tot}^{COPS} measured by the ROSINA-COPS pressure gauge, assuming a mean cometocentric distance for the nucleus' surface of 1.7 km³⁹ and the neutral composition derived from the ROSINA-DFMS mass spectrometer.

Table 2: **Water column density for the limb cases.** Are given the period Px selected, the date, the time range of Px (corresponding to the sub-mm observing period), the value C^{limb} of the water column density used for the calculation of the FUV brightness (see Figure 3), based on the measurements of the column density by the MIRO high-resolution spectrograph in the sub-mm (C^{MIRO}), by the IR high-resolution spectrometer ($C^{VIRTIS-H}$) and by the medium-resolution imaging spectrometer ($C^{VIRTIS-M}$). When no data is available, the column density entry is left blank. The remote-sensing IR measurements are made over approximately the same time range as the sub-mm observations (third column), though there are sometimes some departures in terms of the start or end times (up to 15 min) between instruments.

18-19 October 2014						
Selected period	Day	Time range (UT)	C^{limb} (10^{15} cm^{-2})	C^{MIRO} (10^{15} cm^{-2})	$C^{VIRTIS-H}$ (10^{15} cm^{-2})	$C^{VIRTIS-M}$ (10^{15} cm^{-2})
P1	18 Oct 2014	15:30 – 17:40	1.4	1.41 ± 0.07		1.6 ± 0.7
P2	18 Oct 2014	18:45 – 21:40	2.0	2.04 ± 0.07		2.1 ± 0.9
P3	18–19 Oct 2014	23:40 – 01:40	2.9	2.87 ± 0.09	2.8 ± 0.2	3.4 ± 1.4
P4	19 Oct 2014	02:50 – 05:40	1.1	1.14 ± 0.06		
22-23 October 2014						
P1	22 Oct 2014	15:10 – 17:40 ^a	1.9	1.85 ± 0.08		2.0 ± 0.8
P2	22 Oct 2014	18:45 – 21:40 ^b	1.7	1.68 ± 0.07		1.9 ± 0.8
P3	22–23 Oct 2014	23:40 ^b – 01:40	1.4	1.38 ± 0.10		2.1 ± 0.9
P4	23 Oct 2014	02:40 – 05:40	1.1	1.10 ± 0.06		1.2 ± 0.5

^a The HI Ly β brightnesses over P1 on 22 October 2014 are calculated up to 17:25 UT (see Figure 3b), as the differential flux from the electron spectrometer is not reliable for the rest of P1. ^b The HI Ly β brightnesses over P2 and P3 on 22 October 2014 are calculated up to 22:00 UT and from 23:10 UT, respectively (see Figure 3b) in order to show the trend driven by the variability in the measured differential electron flux.

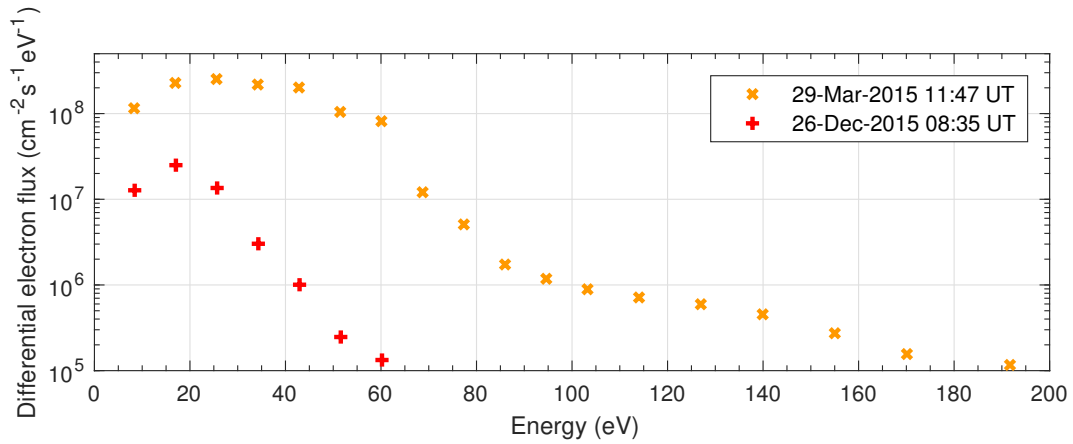


Figure 5: **Extended Data Fig.1. Examples of differential electron fluxes measured by the RPC–IES electron spectrometer and used in the multi-instrument analysis.** The fluxes were observed at 11:47 UT on 29 March 2015 (orange crosses) and at 08:35 UT on 26 December 2015 (red pluses) during two nadir-viewing FUV observation periods. The fluxes are corrected for the spacecraft potential³⁰ (–2 V). By integration, the number density and mean energy of electrons with energies between 10 eV and 200 eV are derived and given in Extended Data Table 1.

Table 3: **Extended Data Table 1. Examples of Rosetta simultaneous measurements.** This dataset has been used for calculating the FUV atomic emission brightnesses at two times during FUV nadir-viewing observation periods (fourth and fifth cases in Figure 2): (1) the differential electron flux J_e (see Extended Data Fig.1) measured by the RPC–IES electron spectrometer at the selected day and start time t^{IES} (first and second columns), at a cometocentric distance r_R (third column), and associated with a number density n_e^{IES} (fourth column) and mean energy E_e^{IES} (fifth column) of electrons with energies between 10 eV and 200 eV; (2) the total neutral density n_{tot}^{COPS} measured by the ROSINA–COPS pressure gauge (sixth column) from which the column density C^{COPS} is derived (seventh column); (3) the neutral composition measured by the ROSINA–DFMS neutral mass spectrometer and given in terms of volume mixing ratio v_n of the four major neutral species (eighth column).

Selected day	t^{IES}	r_R	n_e^{IES}	E_e^{IES}	n_{tot}^{COPS}	C^{COPS}	v_n^{DFMS}
	(UT)	(km)	(cm^{-3})	(eV)	(cm^{-3})	(10^{15} cm^{-2})	H ₂ O, CO ₂ , CO, O ₂ (%)
29 Mar 2015	11:47:18	92	30 ^a	31 ^a	12.5×10^6	6.2 ^b	96, 1.4, 1.6, 1.0 ^c
26 Dec 2015	08:35:08	79	1 ^a	20 ^a	13.5×10^6	4.9 ^b	95, 2.5, 1.1, 1.4 ^c

^a The number density n_e^{IES} and mean energy E_e^{IES} of electrons with energies between 10 eV and 200 eV are derived by integrating the differential electron flux J_e (corrected for the spacecraft potential) over the velocity space. These quantities are given for information; only J_e , not its moments, is used in the calculation of the modelled FUV brightnesses. ^b The total column density is derived from the total neutral density n_{tot} assuming a mean cometocentric distance for the nucleus' surface of 1.7 km. ^c The volume mixing ratio for the four major neutral species is obtained from the ROSINA/DFMS mass spectrometer (other species are neglected).